UNIVERSITY OF CALIFORNIA
RIVERSIDE

Analysis of Transitions in Sperm Motility

A Thesis submitted in partial satisfaction
of the requirements for the degree of

Master of Science

in

Bioengineering

by

Carla Gabriela De Los Santos

August 2015

Thesis Committee:
Dr. Richard Cardullo, Chairperson
Dr. Bahman Anvari
Dr. Valentine Vullev

The Thesis of Carla Gabriela De Los Santos is approved:

Committee Chairperson

University of California, Riverside

Table of Contents

List of Figures

List of Tables

1. Introduction

1.1 Statement of the Problem

The purpose of this research project is to quantitatively describe the physical behavior observed of *Culex pipiens* sperm from motility activation to full motility. The molecular events responsible for key flagellar transitions have recently been described in one species of mosquito, *Culex quinquefasciatus* (Thaler et. al., 2013), allowing for eventual connections to be made between signaling events and biomechanical consequences of those events. However, a true quantitative description of that behavior is currently lacking. Ultimately, understanding the signals and downstream effects is important for understanding the nature of microtubule based machines (e.g., eukaryotic cilia and flagella) that has potential implications for understanding issues related to human fertility, mucus transport, the development of novel contraceptives, and investigations into biomimetic devices.

The quantitative information obtained during the generation of flagellar waveforms provides insight into the underlying patterns of the mechanism behind sliding of the flagellar microtubules by the molecular motor complex, dynein, which together are responsible for the generation and propagation of the oscillations observed during sperm motility (Satir, 1965; Sleigh, 1968; Gibbons, 1974; Goldstein, 1976, 1977, 1979; Brokaw, 1979; Gibbons, 1981).

1.2. Sperm Architecture

1.2.1. Ground Plan "9 + 2"

All flagella are built on a basic design (a ground plan) known as the axoneme that, with few exceptions, is composed of 9 microtubule doublets surrounding a central pair of microtubules (Figure 1). This structure is the basic motility unit that consists of a polypeptide motor complex (dynein) that hydrolyzes ATP and interacts with adjacent microtubules resulting in the relative sliding of adjacent doublet microtubules resulting in a flagellar beat. The beat is harmonic in nature (approximated as a sine function) and is characterized by parameters including a characteristic spatial frequency, amplitude, beat frequency, and wavelength. The propulsive force provided by this machine results in a progressive velocity of the sperm cell that can vary from a few microns per second to hundreds of microns per second (Turner, 2003; Gaffney et. al., 2011).

Much of the early work on understanding the nature of flagellar beating was performed in sea urchin sperm (Afzelius, 1954; Brokaw, 1990). Compared to most sperm, the sea urchin sperm flagellum is remarkably simple and is composed of the basic axoneme surrounded by the plasma membrane. The entire cell is similarly simple in design (Figure 2) and morphologically is made up of a simple head (containing the haploid nucleus, a secretory vesicle known as the acrosome, and one large mitochondrion) and a tail (the flagellum). The tail extends from the base of the head, extending to roughly 50 μm (Afzelius, 1954), and tapers down to the end piece, which constitutes a small fraction of the tail. The compartmentalization of the energy source (mitochondrion) at the head/tail junction along with an array of sinks along the flagellum (the ATPase motors, dynein) allowed investigators to bioenergetically model the simple sea urchin flagellum (Nevo and Rikmenspoel, 1971; Tombes et al., 1984). Although the

sea urchin sperm provided a convenient model for understanding the basic workings of the axoneme, most sperm (including those of mammals and insects) are markedly more complex with the addition of mitochondrial arrays, accessory fibers, and additional rows of microtubules (Lindemann, 1996; Werner and Simmons, 2008; Inaba, 2011).

1.2.2 Modifications to the Basic Flagellar Plan in Mammalian and Insect Sperm

Among animal taxa there is incredible diversity in sperm structure and this is seen in the structure of the motile apparatus, the flagellum, as well (Retzius, 1909; Cummins and Woodall, 1985; Cardullo and Baltz, 1991). The addition of numerous accessory structures most certainly alter the motile behavior of sperm as they encounter different environments and potentially provide a significant viscoelastic element to the flagellum. In mammalian sperm, the tail consists of a midpiece that contains numerous mitochondria surrounding the flagellum for some length and a principal piece that is devoid of mitochondria (Figure 3). There is also an axoneme that is surrounded by a fibrous sheath, except for the end piece (Fawcett, 1975). In addition to the tail, head shapes vary widely in mammalian sperm (Retzius, 1909) from roughly spherical (e.g., guinea pig), oblate ellipsoid (e.g., human, rabbit, and bull), to crescent (e.g., mouse and rat). The combinations of these elements in both the head and tail regions, most certainly have profound consequences in flagellar bioenergetics and biomechanics but these are mostly unexplored.

Insects are the most diverse animal taxa with millions of extant species and this diversity is reflected in sperm structure and function as well (Werner and Simmons,

2008). The general insect sperm ground plan consists of a head, a centriole adjunct, flagellum, and the end piece (Philipps, 1970; Werner and Simmons, 2008; Figure 4). The flagellum consists of the axoneme, mitochondrial derivatives, and accessory bodies. Unlike the mammalian midpiece, the mitochondrial derivatives are comprised of fused mitochondria with little or no cristae and extend longitudinally down the length of the majority of the flagellum. The axoneme also differs in insect sperm, with an additional row of microtubules surrounding the canonical "9+2" array and is classified as a "9+9+2" arrangement of microtubules. Accessory bodies, which are composites of coiled fibers and granules that differ in shape and size within species (Ochs, 1994; Werner and Simmons, 2008), also span the same length as the mitochondrial derivatives, also surrounding the axoneme. The size and shape of the accessory bodies differ in different insect orders (Werner and Simmons, 2008). As with mammalian sperm, the addition of these structures most certainly impacts flagellar bioenergetics and behavior and understanding sperm motility is the major focus of this thesis.

1.3 Activation of Insect Sperm Motility

Sperm activation in sperm has not been widely studied in insects, however, sperm from a number of insect species have been activated using accessory gland secretions and through the use of trypsin-like proteases. This was revealed in early studies focusing on Lepidoptera (Leopold, 1976), with initial studies on the silkworm *Bombyx mori* (Omura, 1936; 1938). In addition, the activation of sperm motility was also studied outside this order in Orthopterans, showing similar activation through the use of trypsin (Osanai and

Baccetti, 1993). Although other methods of activation, such as the presence of oxygen, have been studied the precise mechanisms have not been elucidated (Werner and Simmons, 2008). Recently, the molecular pathways that are responsible for sperm activation in some insect models downstream from protease treatment have been proposed. Studies by Miyata et al., (2012) and Thaler et. al. (2013) showed that sperm motility in insects such as the water strider *Aquarius remigis* and the mosquito *Culex quinquefasciatus* are activated by trypsin-like proteases found in accessory gland secretions and a model representing the signaling cascade has been devised (Miyata et. al., 2012; Thaler et. al., 2013).

1.3.1 Water Strider Sperm

In the semiaquatic insect *Aquarius remigis*, commonly known as a water strider, it was shown by Miyata et al. (2012) that sperm could be activated by a trypsin-like serine protease. The activation was shown to occur through a protease activated receptor 2 (PAR2) and motility and wave formation are a result of MAPK activity (Miyata et. al., 2011). In addition, it was found that Ca^{2+} also plays a requisite role in motility activation. The combination of trypsin-activation of the PAR 2 receptor followed by an increase in intracellular concentration of Ca^{2+}, are responsible for activating flagellar activity.

1.3.2 *Culex quinquefasciatus* Sperm

In *C. quinquefasciatus*, it was also observed that trypsin like proteases and Ca^{2+} had an effect on activation and motility of the sperm (Thaler et al., 2013). The sperm

were activated with either secretions from the accessory glands or the use of trypsin. Once activated, the sperm underwent a series of waveform transitions, these waveforms were categorized into three distinct waveforms: A, B, and C, respectively (figure 5). Once activated, a MAP Kinase pathway is necessary for the transition between waveforms B and C, which leads to a rapid progressive sperm motility (figure 6).

In addition to trypsin and the MAPK signaling cascade, Ca^{2+} was discovered to play a role in the direction of swimming, along with the phosphatase inhibitor okadaic acid. When Ca^{2+} concentration increased, the sperm showed the typical forward motility observed during activation. However, when the concentration of Ca^{2+} was depleted, some of the sperm exhibited backwards swimming. When the phosphatase inhibitor okadaic acid was added in combination, all of the sperm exhibited backwards swimming (figure 6). The latter suggested that a phosphatase inhibitor might also play a role in initiation of motility in sperm for *Culex*.

1.4 Flagellar Biomechanics and Bioenergetics

1.4.1 Resistive Force Theory vs. Slender Body Theory

In the 1950's Gray and Hancock developed a mathematical model for predicting sperm velocity, known as resistive force theory (RFT). Initiation of the theory by Gray was a result of studying snakes and his understanding of undulatory systems; this was later applied and developed for flagellated microswimmers, specifically the sperm of sea urchins (Gray, 1953; Gray and Hancock, 1955). The theory considered the theory of Stokes flows for microswimmers and low Reynolds numbers and improved upon the

current method of sperm parameter measurements at the time, which were based on methods developed by Taylor (Taylor, 1951; Taylor 1952; Rodenburn et. al., 2012). In addition, the mathematical complexity of sinusoidal swimming patters were computed and simplified adapted for RFT by Hancock (1953).

In RFT the hydrodynamic forces are proportional to the local body velocity, with the constant of proportionality defined as the drag force coefficient, which is the key factor in predicting the velocity of motile sperm. The different and opposing forces acting on a small section of the flagellum can be broken down and with assumptions regarding the coefficients of drag the following mathematical model was proposed:

$$\overline{V_x} = \frac{2f\pi^2 b^2}{\lambda}\left\{\frac{1}{1+\frac{4\pi^2 b^2}{\lambda^2}-\sqrt{\left(1+\frac{2\pi^2 b^2}{\lambda^2}\right)}\frac{3a}{n\lambda}\left[\left(\log\left(\frac{d}{2\lambda}\right)\right)+0.5\right]}\right\}$$

Where

$\overline{V_x}$ is the forward velocity of the sperm

f is the flagellar beat frequency

b is the flagellar amplitude

a is the radius equivalent of an Oblate ellipsoid

d is the radius of filament

n is the number of waves exhibited by the flagellum

λ is the wavelength of the waveform generated by the flagellum

Subsequent to the development of RFT, Cox and Batchelor separately contributed to the development of slender body theory (SBT) as a method of modeling microswimmers in viscous fluids (Cox 1970; Batchelor, 1970). The theory itself was originally conceived by Burgers in 1938 and was advanced by others including Tuck (1964, 1970), Taylor (1969), and Tillett (1970). In addition to this, Lighthill (1970) contributed to the simplification of the theory, while Johnson (1977) fully developed what is now the SBT. SBT served as a more general approach that would also result better accuracy. The theory also focuses on modeling slender filaments swimming in viscous fluids.

In SBT the flagellar motions of large amplitude waves are expected to be the principal factor in generating flow fields. Theories for predicting key motility parameters of microswimmers must consider effects of the presence of a cell body attached to one end of the flagellum, which modifies the flow field experienced by the flagellum. This interaction, which is not considered in resistive-force theory, is insignificant for small cell bodies, such as the heads of simple spermatozoa, but limits the accuracy of the theory for larger cell bodies, or cell bodies that have large-amplitude motions transverse to the swimming direction, which require the use of slender-body theory for accurate analysis (Johnson and Brokaw, 1979).

1.4.2 Examples of Sperm Measured by RFT and SBT

In the original development of resistive force theory, sea urchin sperm were used to test the theory. Sperm parameters were measured as accurately as possible with the

limited technology available during the time and resulted in a remarkably accurate prediction of the sperm velocity. Although this was attributed to luck at the time, the theory remained an accurate and simple method of predicting sperm velocity (Gray and Hancock, 1955).

A more recent example of testing resistive force theory was performed on bull sperm. Using high precision measurements necessary to predict sperm velocity and high precision tracking of actual sperm velocity, researchers looked at the sperm trajectory during different times and found the theory to accurately predict the observed motility behavior (Friedrich, 2010).

1.4.3 Metabolism and The Role of the Mitochondria

Flagellar motion caused by the bending of filaments found along the flagellum is an active process and requires energy. The energy necessary for this process is stored as ATP, which is produced either anaerobically through glycolysis or aerobically through oxidative phosphorylation coupled to respiration. ATP that is synthesized aerobically has been seen in mammalian and echinoderm sperm, specifically in bull and sea urchin sperm. This process takes place in the mitochondria, which is located next to the base of the head. Mitochondria work to produce ATP necessary for motility. The ATP is transported from the mitochondria to the axoneme by a phosphorylcreatine shuttle, which relies on a mitochondrial and an axonemal creatine kinase to diffuse the ATP necessary to maintain flagellar activity (Nevo and Rikmenspoel, 1970; Tombes and Shapiro, 1985).

1.4.4 Sea Urchin Sperm Metabolism

Sea urchin has been a widely studied model for sperm motility, including the metabolism aspect involved. In sea urchin sperm, studies regarding ATP concentration during sperm beating resulted in the discovery that beat frequency has a Michaelis Menten type of relationship to ATP concentration (Brokaw, 1967). Another major discovery for the relationship of motility and metabolism in sea urchin sperm showed that the ATP dephosphorylation is coupled to motility, this was seen in studies using demembranated spermatozoa (Brokaw, 1968).

1.4.5 Biomechanics and Bioenergetics

Production of energy required for sperm motility has been studied in different species in relation to biomechanics. Given the interest in the production of power, its synthesis, and its role in motility, there are alternative methods to understand the bioenergetics demands on sperm through biomechanics and modeling. The observed physical behavior of sperm, along with the measured key parameters, can be used to determine the power output of the sperm flagellum. Cardullo and Baltz (1991) devised a relationship between power production and power output in mammalian sperm. Using key parameters, such as frequency and flagellar length, one can calculate the power output, which can show what is going on at the biochemical level when a sperm is swimming at different velocities.

1.4.6 Insect Sperm Biomechanics

Sperm flagellar structure varies amongst insects, as previously mentioned. Current knowledge of sperm biomechanics is heavily based on sperm exhibiting simpler waveforms, such as planar waves, even though there are species that generate waveforms that fall under the double wave description (Werner and Simmons, 2008; Pak et. al, 2012; Thaler et al., 2013).

1.5 Resistive Force Theory and Mosquito Sperm

Given the accuracy of resistive force theory using imaging technologies that allow for more precise measurements of key motility parameters, resistive force theory can be applied to sperm that exhibit planar motion and share similar motility patterns to sea urchin sperm. Mosquito sperm provide one such system and has the added benefit of exhibiting different behaviors (e.g. waveforms A, B, and C) that can be studied using resistive force theory.

2. Materials and Methods

2.1. Sample Preparation

Male *Culex pipiens* mosquitoes were kept in small plastic cups with lids. Each cup housed 1 mosquito and contained diluted sugar to serve as nutrients and contribute to humidity. When the mosquito was ready to be dissected, a small piece of cotton was soaked in chloroform and quickly placed inside the cup and the lid was secured. The sperm was kept in the cup for about 2-5 minutes and then transferred to a well on a dissecting plate that contained a drop of phosphate buffered saline (PBS). The PBS solution consisted of 135 mM NaCl, 10 mM Na_2HPO_4, and 2 mM NaH_2PO_4 and had a pH 7.2. The mosquito was dissected under a Leica Wild M3Z stereomicroscope. Seminal vesicles and accessory glands were removed while in a PBS solution. They were then transferred to a glass slide in about 20 μm of insect ringer solution. The rest of the mosquito was discarded. A cover slip was placed gently over the area where the drop of Insect Ringer, seminal vesicle, and accessory glands were located. Pressure was applied to the cover slip in order to break open accessory glands and seminal vesicles. The sperm were activated by a combination of Insect Ringer and the accessory gland secretions that made up the swimming medium. In cases focusing on sperm undergoing waveform A, only the seminal vesicle was removed from the mosquito. The same process was followed, but Insect Ringer was used instead of the accessory glands to so that the sperm would remain in waveform A as described in Thaler et. al (2013).

2.2. Motile Sperm Image Acquisition

Activated sperm on glass slide were observed using a Nikon Labphot Microscope at 10x or 20x magnification. The 10x magnification was used to get a larger field of view when observing sperm motility. This made it possible to get a large enough image to identify the waveform and other key motility and flagellar parameters while still being able to observe sperm swimming behavior for long periods of time to accurately calculate beat frequency and forward velocity. In contrast, the 20x magnification was used to get more accurate measurements of sperm morphology such as the head dimensions, the sperm length, and the width of the flagellum. The length of the mosquito sperm at 20x took up most of the field of view. Phase contrast microscopy was the method of choice due to the defined boundaries around the cell that allowed for more accurate determinations of dimensions and reducing measurement error.. Sperm were recorded using Scion Image software and a DAGE-MTI CCD100 camera at a frame rate of 30 frames/second. Sperm recordings were saved as Tiff stacks and saved for additional image processing.

2.3 Image Processing and Measurements

The file was opened using the ImageJ image processing software, an open source software package produced and distributed by the National Institute of Health. Upon opening the image, the scale was set by using a micrometer scale for corresponding magnification and selecting the 'global' option. The conversion was from 100 μm to 124 pixels (1.24 pixels/ μm) for a 10x magnification file. After the scale was set to

micrometers, the stack file containing sperm data was viewed in order to identify potential waveforms. Once the waveform of interest were identified, in this case A and C, the file was further broken down into smaller clips showing only the waveform of interest for its entire run in the field of view (occasionally there was more than one sperm undergoing the specific waveform). The 'duplicate' option was used to reproduce identical portions of interest within the original file, since the first rule of thumb in working with files is to always keep a back up of the original. Once the waves were broken down into smaller files, this took up less memory allowing for the video to run smoothly and did not distract from the waveforms being observed.

Once the waveforms were identified, the velocities of each sperm were measured to make sure the velocity associated with the waveform matched. For wave A, the velocity was required to be a maximum 10 μm/sec and for wave C, the velocity range was a minimum of 65 μm/sec. If the velocity was with the range for the particular waveform, the waveform clips were then processed using the ImageJ image processing toolbox. The main objective during image processing was to get a clear and clean representation of the sperm. The first step was to remove background that consisted of static images; this was done using a modified version of a macro for removing static background from avi files developed by Collingridge (2010) to recognize Tiff files instead of avi.

Once the specific image stack sequence was selected I adjusted the image contrast/brightness and then adjusted the threshold to convert it into a binary image. Converting the image to binary enabled me to use a number of binary processing tools including: dilate, close, fill holes, skeletonize (order performed varies on stack). Other

processing tools were used to minimize shot noise such as the despeckle function. The final processed image resulted in a binary image of the sperm of interest, which could then be used to measure parameters.

Parameters were measured using the ImageJ line tool and the multipoint function. The sperm velocity of the head was measured by calculating the distance between two points: the first frame in a series of the head using the multipoint tool and then a second point after at least 90 frames. The coordinates of the two points were determined using the measure tool. The distance between these two points was then calculated using the distance formula and then divided by the number of seconds of footage being analyzed. The velocity was calculated by using the distance divided by the elapsed time (calculated as the number of frames collected divided by the frame rate (30 frames/ second)).

The amplitude was measured using the skeletonized sperm, which showed distinct waveforms. The amplitude was measured from an approximate midpoint in middle of wave from middle peak to trough with the line tool at 0 degrees. The sperm was rotated to sit on a 0 degree line and, the measurements were then taken for each amplitude (peak/ trough) at 90 degree straight line from 0 degree line to the top of the peak or bottom of trough. These amplitudes were than averaged to obtain a mean value for the amplitude.

The wavelength was measured using line tool from peak-to-peak or trough-to-trough, depending on what was shown on the wave and easier to measure.

The frequency was measured by going through the stack, choosing a frame, and then going through the stack to see where the waveform repeated through a visual estimation of a complete cycle. This was done visually with duplicating the waveform

frame of reference and going through the stack. Next, the number of frames to repeat the waveform was calculated and converted to a frequency using the frame rate at which the video was recorded (figure 7).

2.4. Statistical Analysis

Statistical Analysis was performed using StatPlus:mac software distributed by AnalystSoft Inc. The software was used to perform an Analysis of Variance (ANOVA) on the sperm samples collected for each waveform for the predicted and calculated velocities shown in figures 13 and 14.

3. Results

3.1 Measurements of Waveform Parameters

Following the same protocol as for *C. quinquefasciatus* sperm, the sperm for *C. pipiens* were activated in Insect Ringer with accessory gland secretions. Using a light microscope at 10x magnification to view the sperm, the observed sperm were active and rapidly began to transition between the three distinct waveforms as shown in figure 8, similar to that described for *C. quinquefasciatus* sperm (Thaler et al, 2013). The sperm were viewed using video microscopy; specifically phase contrast (section 2) and the recordings were saved and analyzed using ImageJ. The waveforms were categorized by speed, time point, and shape of the waveforms, based on the information provided by Thaler et al. (2013) and unpublished data from the Cardullo lab. The sperm analyzed for this project were restricted to waveforms A and C only.

In order to verify the specific waveform, the velocity was measured to ensure the velocity range matched the wave generated. For Wave A, only values less than or equal to 10 μm/s were considered while only values above 65 μm/s were considered for Wave C.

The data was collected for 16 individual sperm cells from at least 5 different animals, for each waveform (Table 2). The morphological parameters for the sperm head, modeling it as an ellipsoid, were also collected for 30 individual sperm cells from at least 5 different samples (Table 3).

The parameters necessary for determining forward velocity using resistive force theory (Gray and Hancock, 1955) are listed and defined in Table 1. The parameters were

measured using sperm recordings of Wave A and Wave C motility patters and processed using ImageJ. A comparison of the resulting parameter measurements for waveform A and C can be seen in figures 9 – 11; such parameters include amplitude, beat frequency, and wavelength, respectively.

3.2 RFT Equation and Modifications

3.2.1 Resistive Force Theory Proposed by Gray and Hancock

Using the model for sperm velocity based on propulsive force by Gray and Hancock, the equation in section 1.3.1 was used as a starting point to test the theory using key sperm parameters measured from the sperm of *C. pipiens*:

$$\overline{V_x} = \frac{2f\pi^2 b^2}{\lambda}\left\{\frac{1}{1+\frac{4\pi^2 b^2}{\lambda^2}-\sqrt{(1+\frac{2\pi^2 b^2}{\lambda^2})}\frac{3a}{n\lambda}\left[\left(\log\left(\frac{d}{2\lambda}\right)\right)+0.5\right]}\right\}$$

This equation approximates the shape of the sperm head as a spheroid and was used for the study to account for the drag of the head; this is noted by the radius of that sphere and defined as a in the equation.

3.2.2 Modification for Spheroid vs. Ellipsoid Head

Since the head of the mosquito sperm is an ellipsoid, I modified the RFT equation to more accurately reflect that head shape. Consequently, hydrodynamic theory was used to substitute make a modification to a as follows:

$$a = \frac{(j)\sqrt{(1-p^2)}}{\sqrt[3]{(p)}\tan^{-1}(\frac{\sqrt{(1-p^2)}}{p})}$$

where

$$p = \frac{h}{j}$$

and

$$h = minor\ axis$$

$$j = major\ axis$$

The rest of the equation proposed by Gray and Hancock remained unchanged.

3.2.3 Prediction of Sperm Velocity for Waveforms A and C

Before using the equation for velocity using resistive force theory, the measured velocities for waveforms A and C were compared and used as reference values for predicting velocity (Figure 12). Prediction of sperm velocity was performed using both the original equation (3.2.1) and the modified equation (3.2.2) for both waveforms, the resulting data collected can be seen in figures 13 and 14. Both equations predicted a noticeable difference between the velocities of waveform A and C, consistent with the measured velocities.

The velocity predicted for waveform A (figure 12) for both ellipsoid and spherical heads were below 2-fold of the measured velocity. The velocity predicted for the spherical head over estimated the measured velocity at 1.18 fold, while the ellipsoid head showed a 1.53 fold difference in velocity. The comparison between the measured and calculated velocities fore waveform A were not statistically different based on their p value from the ANOVA analysis.

For waveform C, the velocities predicted using resistive force theory and the measured parameters also followed similar results (figure 13), where the spherical head showed a closer prediction to the measured velocity than the equation using the ellipsoid head. The results for both forms of the equation were within a 5-fold difference from the measured velocity with the spherical head showing about a 2.74 fold difference and the ellipsoid head about a 4.9 fold difference, both under predicting the measured velocity. The comparison between the measured and the calculated velocities fore waveform C were statistically different based on their p value from the ANOVA analysis.

4. Discussion

4.1 Relevance to Mosquito Sperm

It has been shown that changes in waveforms in activated sperm are important for successful fertilization in different animal systems (Thaler et. al, 2013), making the progression through the three waveforms potentially important to *C. pipiens*. Identical to the findings previously discovered in *C. quinquefasciatus* (Thaler et. al, 2013), *C. pipiens* sperm undergo transition from an immotile state and then progress through waveforms A, B, and C when activated by accessory gland secretions.

The sperm from *C. pipiens* can be a model organism based on the underlying axonemal structure that is seen in all flagellated sperm but, unlike other insects studied to date, the reproducible and sequential motility patters allow for detailed biomechanical analysis to be performed. Mosquitoes are of biological interest since they are pests and serve as vectors for numerous pathogens. With the recent model developed for protease-activated sperm for *C. quinquefasciatus* (Thaler et al., 2013), it is likely that the molecular pathways leading to sperm motility activation and progression of *C. pipiens* and *C. quinquefasciatus* are similar.

4.2 Relevance to Human Sperm and Other Motile Cells

The system used for this experiment allows for quantification of key wave parameters, and parameters that can be used not only to model the velocity of the sperm, but also to obtain useful information on other biophysical parameters of sperm motility behavior. The biophysical parameters that change between the molecular switching

events during sperm motility and in wave generation have yet to be described in any studies thus far.

Sperm from mammals differs in structure and components from other species, there is a general theme identified in sperm cells that they exist in an immotile state until activated and motility ensues. The similarities in this behavior imply that signaling pathways exist for sperm, which can be explained and better understood by relating the physical behavior to the molecular events that take place during and through activation of sperm. Although sperm from mammals undergo transitions and molecular events that seem more complex than those observed in *Culex* mosquitos, such as that mammalian sperm are stored in the vas deferens and are immotile until entering the female reproduction tract. They become activated in the female reproductive tract, where they encounter rheological environments and eventually undergo capacitation, which is essential for sperm-egg recognition. During capacitation, which does not occur in insects, the sperm also undergo a change in motile behavior to what is described as hyper activation, which allows for the change in sperm velocity and beat frequency necessary for the sperm to more efficiently reach the egg (Tulsiani and Abou-Hail, 2012). Understanding the link in mosquito sperm can serve as groundwork for a full understanding of the mechanism of sperm motility in other species in a more simplified manner.

Using the key parameter measurements necessary for sperm, the measured information can also be used to relate the physical behavior to the molecular behavior by looking at the bioenergetics and biomechanics of the sperm undergoing the different

waveforms. As seen in Cardullo and Baltz (1991) for rat sperm, using the information collected, the power output for each waveform can be calculated using their model predicting power output for a beating flagellum. From that model, for a waveform A at the average frequency of 1.59 (table 2), the power output generated by this waveform is 2.3×10^{-7} ergs/sec, while not surprising for waveform C, which consists of a higher frequency at 4.16 Hz (table 2), the power output results in 16×10^{-7} ergs/sec. This information can be used to theorize the ATP consumption of the motile sperm undergoing each waveform, which when converted from the power output results, waveform A consumption rate is roughly 4.4×10^{5} ATPs/sec and for waveform C is 3.0×10^{6} ATPs/sec. Knowing the ATP consumption allows us to gain insight on what is necessary for motility and each waveform and possibly how the molecular motor itself is working, specifically how many dynein's are present and their rate of ATP turnover.

Another aspect of the Power output and predicted ATP consumption can result in the understanding of other sources of ATP that can provide enough to allow a sperm cell to become motile, since mosquito sperm do not contain a functioning mitochondria such as the one present in mammalian sperm. Looking at the factors necessary for activating the sperm motility in vitro for Culex sperm, glucose is present in the medium necessary for activation, which could result in glycolysis being a method of energy production in sperm not containing functioning mitochondria. Previous studies have shown that glycolysis is a possible method of ATP production in sperm, and the components necessary to use glycolysis exist in the principle piece for mammalian sperm (Visconti, 2012).

4.3 General Importance

The sperm is an example of a natural occurring mechanical motor at a nanoscale (Taylor and Holwill, 1999) and the ability for this to successfully enter a body without an immune response has therapeutic potential in humans. The evolutionarily conserved machine, the axoneme, has also been of interest for nanorobotics, the eukaryotic flagellum in an efficient swimmer and a nanoscale. For these reasons it is important to fully understand the mechanism of sperm motility (Lauga and Powers, 2009; Tabak and Yesilyurt, 2013)

4.4 Application of Basic Theory and Measured Key Flagellar Parameters

From the data obtained from sperm measurements and the predictions made using RFT, waveforms A and C show a difference in key parameter values that agree with the distinctions made by Thaler et. al.e (2013). The waveforms demonstrate a sine wave when observed in a 2 dimensional plane that contains slightly different wave number. One limitation observed for wave A was the amplitudes were often less symmetrical.

For both waveforms, there are also portions, as mentioned in the results, that don't contribute to the waveform. The sperm have a head and an end piece that is stationary, which flank the flagellar portion. Depending on the wave progression, the middle flagellum can form a wave that spans the entire section or just a portion of it, exhibiting more of a pulse like wave, and not necessarily the type of way represented in the current model based on RFT.

The data collected shows that the current model for resistive force theory and the modified version presented in this study can serve as a starting point for quantifying the transition waves A and C based on the key parameters, however, further development of the mathematical model is needed and other aspects of the observed sperm morphology may play a key role in a more accurate prediction of sperm progression.

4.5 Future Directions

Although the data showed that a velocity could be predicted using resistive force theory, the differences between the modified equation and original equation did not show a significant difference to prove the ellipsoid shape of the head could be a more accurate method. Despite the head of the sperm showing an ellipsoid head, the movement during forward progression may result in a more spherical motion produced by the head, which could explain more agreeable results from using a spherical drag. The substitution for an ellipsoid head accounts only for an ellipsoid drag, while the motion of the head in a 3 dimensional perspective may change the direction of the ellipsoid or cause a more circular motion during forward progression, making the ellipsoid drag alone not sufficient for predicting an accurate velocity. Alternatively, other equations do exist that have been proven to predict velocities more accurately resistive force theory, such as Slender Body Theory (SBT) as discussed in section 1.SBT, however, would require the use of mathematical programs to solve systems of equations as well as larger sample size, but has proven to result in accurate velocity predictions (Brokaw, 1979).

In addition to further modifying the RFT model, more analysis on waveform B should also be performed. Although this study did not focus on waveform B, it has been noted by Thaler et. al. (2013) that this waveform may be a transitional state between waveform A and C, which is an important step in the signaling and regulation pathway for sperm motility in Culex sperm. Waveform B consists of two superimposed waveforms and serves as the intermediate waveform from activation (waveform A) and fully activated sperm (waveform C), making this a potential result of the switching events occurring during the identified signaling pathway for *Culex quinquefasciatus*, which is most likely the same in *Culex pipiens*. The final step would be to link the behavioral changes during activation in the flagellum to those identified in the molecular pathway.

.

5. References

Afzelius, B. A. (1954). The fine structure of the sea urchin spermatozoa as revealed by the electron microscope. *Zeitschrift Fur Zellforschung Und Mikroskopische Anatomie* , *42*(1-2), 134–148.

Batchelor, G. K. (1970). Slender-body theory for particles of arbitrary cross-section in Stokes flow. *Journal of Fluid Mechanics*, *44*(03), 419–440.

Brokaw, C. J. (1967). Adenosine triphosphate usage by flagella. *Science*, *156*(3771), 76–78.

Brokaw, C. J. (1979). Calcium-induced asymmetrical beating of triton-demembranated sea urchin sperm flagella. *The Journal of Cell Biology*, *82*(2), 401–411.

Brokaw, C. J. (1990). The sea urchin spermatozoon. *BioEssays: News and Reviews in Molecular, Cellular and Developmental Biology*, *12*(9), 449–452.

Brokaw, C. J. (2006). Flagellar propulsion. 1955. *The Journal of Experimental Biology*, *209*(Pt 6), 985–986.

Brokaw, C. J., & Benedict, B. (1968). Mechanochemical coupling in flagella. I. Movement-dependent dephosphorylation of ATP by glycerinated spermatozoa. *Archives of Biochemistry and Biophysics*, *125*(3), 770–778.

Burgers, J. M. (1995). On the Motion of Small Particles of Elongated Form. Suspended in a Viscous Liquid. In *Selected Papers of J. M. Burgers* (pp. 209–280). Springer Netherlands.

Cardullo, R. A., & Baltz, J. M. (1991). Metabolic regulation in mammalian sperm: mitochondrial volume determines sperm length and flagellar beat frequency. *Cell Motility and the Cytoskeleton*, *19*(3), 180–188.

Collingridge, P. (2010, December 12). Removing background from an AVI using ImageJ. Retrieved August 25, 2015, from http://www.petercollingridge.co.uk/blog/removing-background-avi-using-imagej

Cox, R. G. (1970). The motion of long slender bodies in a viscous fluid Part 1. General theory. *Journal of Fluid Mechanics*, *44*(04), 791–810.

Cummins, J. M., & Woodall, P. F. (1985). On mammalian sperm dimensions. *Journal of Reproduction and Fertility*, *75*(1), 153–175.

Darszon, A., Nishigaki, T., Beltran, C., & Treviño, C. L. (2011). Calcium channels in the development, maturation, and function of spermatozoa. *Physiological Reviews*, *91*(4), 1305–1355.

Fawcett, D. W. (1975). The mammalian spermatozoon. *Developmental Biology*, *44*(2), 394–436.

Friedrich, B. M., Riedel-Kruse, I. H., Howard, J., & Jülicher, F. (2010). High-precision tracking of sperm swimming fine structure provides strong test of resistive force theory. *The Journal of Experimental Biology*, *213*(Pt 8), 1226–1234.

Gaffney, E. A., Gadêlha, H., Smith, D. J., Blake, J. R., & Kirkman-Brown, J. C. (2011). Mammalian Sperm Motility: Observation and Theory. *Annual Review of Fluid Mechanics*, *43*(1), 501–528.

Gibbons, I. R. (1981). Transient flagellar waveforms during intermittent swimming in sea urchin sperm. II. Analysis of tubule sliding. *Journal of Muscle Research and Cell Motility*, *2*(1), 83–130.

Gibbons, I. R. (2013). MECHANISMS OF FLAGELLAR MOTILITY. In *The Functional Anatomy of the Spermatozoon: Proceedings of the Second International Symposium, Wenner-Gren Center, Stockholm, August 1973* (Vol. 23, p. 127). books.google.com.

Goldstein, S. F. (1979). Starting transients in sea urchin sperm flagella. *The Journal of Cell Biology*, *80*(1), 61–68.

Goldstein, S. F. (1977). Asymmetric waveforms in echinoderm sperm flagella. *The Journal of Experimental Biology*, *71*, 157–170.

Goldstein, S. F. (1976). Form of developing bends in reactivated sperm flagella. *The Journal of Experimental Biology*, *64*(1), 173–184.

Gray, J., & Hancock, G. J. (1955). The Propulsion of Sea-Urchin Spermatozoa. *The Journal of Experimental Biology*, *32*(4), 802–814.

Gray, J. (1953). Undulatory Propulsion. *The Quarterly Journal of Microscopical Science*, *s3-94*(28), 551–578.

Inaba, K. (2011). Sperm flagella: comparative and phylogenetic perspectives of protein components. *Molecular Human Reproduction*, *17*(8), 524–538.

Johnson, R. E., & Brokaw, C. J. (1979). Flagellar hydrodynamics. A comparison between resistive-force theory and slender-body theory. *Biophysical Journal*, *25*(1), 113–127.

Johnson, R. E. (1977). *Slender-body theory for Stokes flow and flagellar hydrodynamics*. California Institute of Technology.

Lauga, E., & Powers, T. R. (2009). The hydrodynamics of swimming microorganisms. *Reports on Progress in Physics*, *72*(9), 096601.

Leopold, R. A. (1976). The Role of Male Accessory Glands in Insect Reproduction. *Annual Review of Entomology*, *21*(1), 199–221.

Lighthill, M. J. (1970). Aquatic animal propulsion of high hydromechanical efficiency. *Journal of Fluid Mechanics*, *44*(02), 265–301.

Lighthill, J. (1976). Flagellar hydrodynamics. *SIAM Review*, *18*(2), 161–230.

Lindemann, C. B. (1996). Functional significance of the outer dense fibers of mammalian sperm examined by computer simulations with the geometric clutch model. *Cell Motility and the Cytoskeleton*, *34*(4), 258–270.

Miyata, H., Noda, N., Fairbairn, D. J., Oldenbourg, R., & Cardullo, R. A. (2011). Assembly of the fluorescent acrosomal matrix and its fate in fertilization in the water strider, Aquarius remigis. *Journal of Cellular Physiology*, *226*(4), 999–1006.

Miyata, H., Thaler, C. D., Haimo, L. T., & Cardullo, R. A. (2012). Protease activation and the signal transduction pathway regulating motility in sperm from the water strider Aquarius remigis. *Cytoskeleton* , *69*(4), 207–220.

Nevo, A. C., & Rikmenspoel, R. (1970). Diffusion of ATP in sperm flagella. *Journal of Theoretical Biology*, *26*(1), 11–18.

O'Toole, E. T., Giddings, T. H., Jr, Porter, M. E., & Ostrowski, L. E. (2012). Computer-assisted image analysis of human cilia and Chlamydomonas flagella reveals both similarities and differences in axoneme structure. *Cytoskeleton* , *69*(8), 577–590.

Ochs, R. L., Stein, T. W., Jr, & Tan, E. M. (1994). Coiled bodies in the nucleolus of breast cancer cells. *Journal of Cell Science*, *107 (Pt 2)*, 385–399.

Osanai, M., & Baccetti, B. (1993). Two-step acquisition of motility by insect spermatozoa. *Experientia*, *49*(6-7), 593–595.

Pak, O. S., Spagnolie, S. E., & Lauga, E. (2012). Hydrodynamics of the double-wave structure of insect spermatozoa flagella. *Journal of the Royal Society, Interface / the Royal Society*, *9*(73), 1908–1924.

Pedersen, H. (1969). Ultrastructure of the ejaculated human sperm. *Zeitschrift Fur Zellforschung Und Mikroskopische Anatomie* , *94*(4), 542–554.

Phillips, D. M. (1970). Insect sperm: their structure and morphogenesis. *The Journal of Cell Biology*, *44*(2), 243–277.

Retzius, G. (1909). Spermatozoa of mammals. *Biol. Unters. NF*, *14*, 163–178.

Rodenborn, B., Chen, C.-H., Swinney, H. L., Liu, B., & Zhang, H. P. (2013). Propulsion of microorganisms by a helical flagellum. *Proceedings of the National Academy of Sciences of the United States of America*, *110*(5), E338–47.

Satir, P. (1965). Studies on cilia II. Examination of the distal region of the ciliary shaft and the role of the filaments in motility. *The Journal of Cell Biology*, *26*(3), 805–834.

Sleigh, M. A. (1968). Patterns of ciliary beating. *Symposia of the Society for Experimental Biology*, *22*, 131–150.

Tabak, A. F., & Yesilyurt, S. (2013, November 14). *Hydrodynamic surrogate models for bio-inspired micro-swimming robots. arXiv [physics.flu-dyn]*.

Taylor, G. I. (1951). Analysis of the Swimming of Microscopic Organisms. *Proceedings of the Royal Society of London. Series A, Mathematical and Physical Sciences*, *209*(1099), 447–461.

Taylor, G. I. (1952). The Action of Waving Cylindrical Tails in Propelling Microscopic Organisms. *Proceedings of the Royal Society of London. Series A, Mathematical and Physical Sciences*, *211*(1105), 225–239.

Taylor, G. I. (1969). Motion of axisymmetric bodies in viscous fluids. *Problems of Hydrodynamics and Continuum Mechanics, SIAM Publ*, 718–724.

Taylor, H. C., & Holwill, M. E. J. (1999). Axonemal dynein - a natural molecular motor. *Nanotechnology*, *10*(3), 237.

Thaler, C. D., Miyata, H., Haimo, L. T., & Cardullo, R. A. (2013). Waveform generation is controlled by phosphorylation and swimming direction is controlled by Ca2+ in sperm from the mosquito Culex quinquefasciatus. *Biology of Reproduction*, *89*(6), 135.

Tillett, J. P. K. (1970). Axial and transverse Stokes flow past slender axisymmetric bodies. *Journal of Fluid Mechanics*, *44*(03), 401–417.

Tombes, R. M., & Shapiro, B. M. (1985). Metabolite channeling: a phosphorylcreatine shuttle to mediate high energy phosphate transport between sperm mitochondrion and tail. *Cell*, *41*(1), 325–334.

Tuck, E. O. (1964). Some methods for flows past blunt slender bodies. *Journal of Fluid Mechanics*, *18*(04), 619–635.

Tuck, E. O. (1970). Unsteady flow of a viscous fluid from a source in a wall. *Journal of Fluid Mechanics*, *41*(03), 641–652.

Tulsiani, D. R. P., & Abou-Haila, A. (2012). Biological Processes that Prepare Mammalian Spermatozoa to Interact with an Egg and Fertilize It. *Scientifica*, *2012*, 607427.

Turner, R. M. (2003). Tales from the tail: what do we really know about sperm motility? *Journal of Andrology*, *24*(6), 790–803.

Visconti, P. E. (2012). Sperm bioenergetics in a nutshell. *Biology of Reproduction*, *87*(3), 72.

Werner, M., & Simmons, L. W. (2008). Insect sperm motility. *Biological Reviews of the Cambridge Philosophical Society*, *83*(2), 191–208.

Ômura, S. (1936). Artificial insemination of Bombyx mori. *Journal of the Faculty of Agriculture, Hokkaido Imperial University= 北海道帝國大學農學部紀要*, *38*(2), 135–150.

Ómura, S. (1938). Structure and function of the female genital system of Bombyx mori with special reference to the mechanism of fertilization. *Journal of the Faculty of Agriculture, Hokkaido Imperial University= 北海道帝國大學農學部紀要*, *40*(3), 111–128.

6. Figures

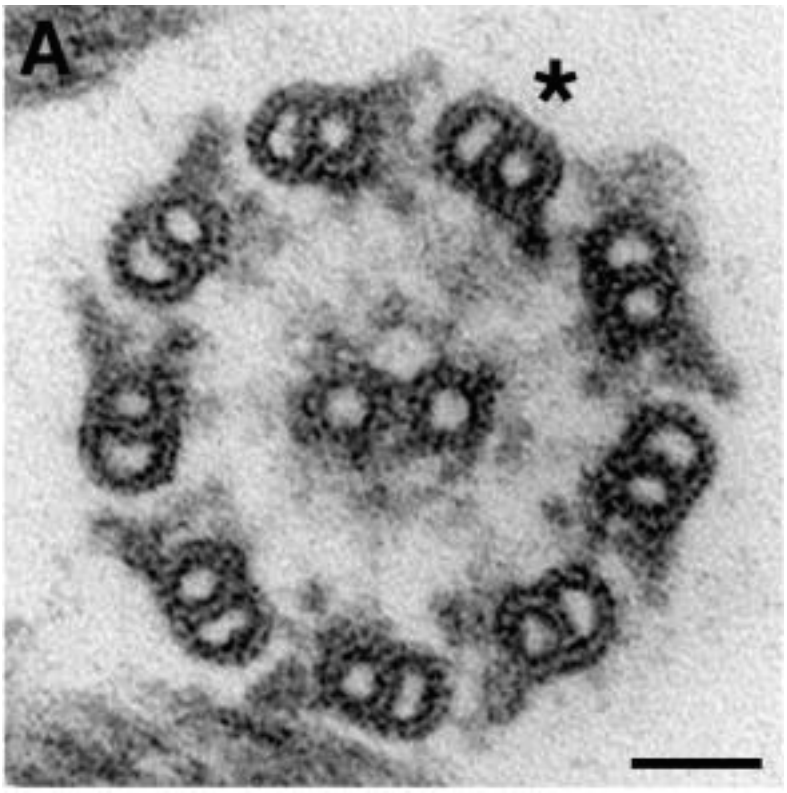

Figure 1 Basic "9 + 2" Plan of Axoneme Structure (O'Toole, 2012).
Chlamydomonas axoneme cross section showing the typical 9 +2 arrangement of outer microtubule doublets surrounding a central pair complex. The doublet microtubules contain attached inner and outer dynein arms with doublet number one missing the outer arm (*). Bar = 50 nm.

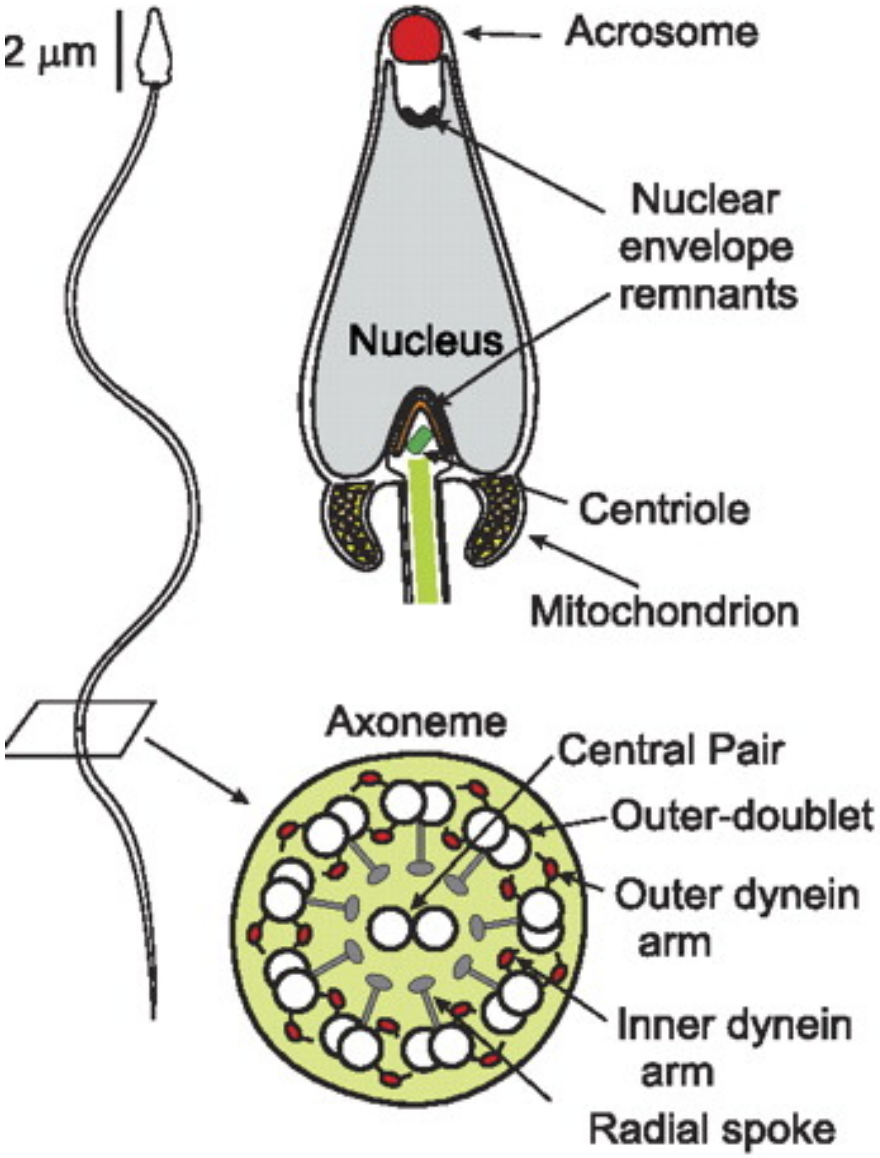

Figure 2 Schematic Representation of the Sea Urchin Sperm Cell (Darszon, 2011). Left: the sea urchin sperm cell body. Top right: the sperm head cross-section showing the location of the acrosome, nucleus, centriole, and nuclear envelope remnants as indicated by the arrows and the text. Bottom right: the cross-section of flagellum depicting the typical 9 + 2 axoneme structure.

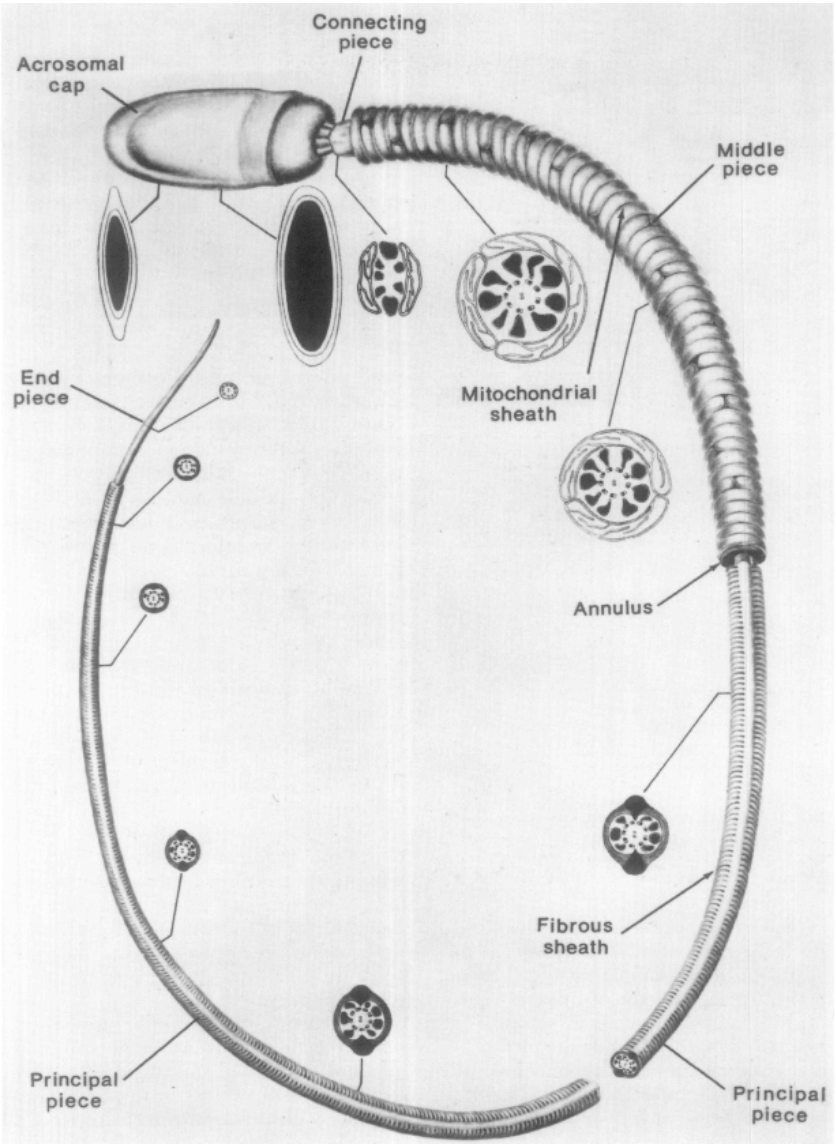

Figure 3 Schematic Representation of the Mammalian Sperm Cell (Fawcet, 1975). Illustrated general mammalian sperm cell. This shows the different structural components of the sperm beneath the cell membrane.

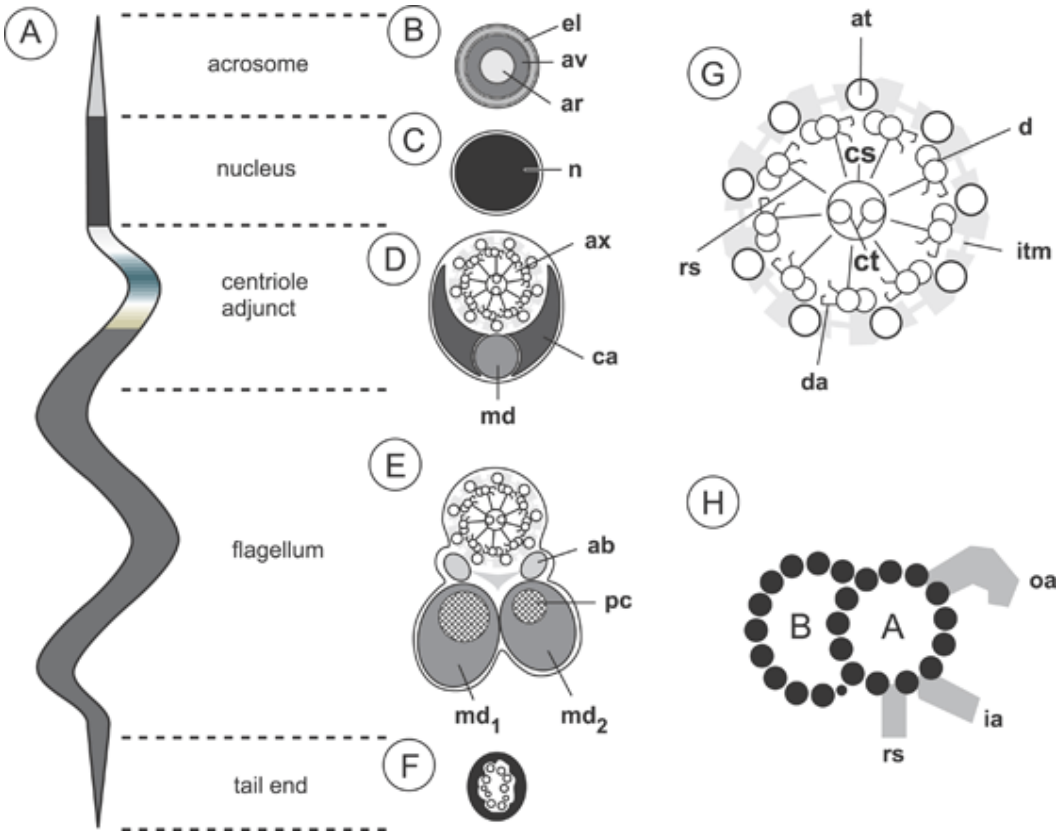

Figure 4 Schematic Representation of Insect Sperm Structure (Werner and Simmons, 2008). Shows the ground plan of a pterygote insect flagellosperm and its ultrastructure. (A) Overview of a pterygote insect sperm cell. (B) Cross section of the acrosome. (C) Cross section of the nucleus (n). (D) Cross section of the posterior centriole adjunct region. (E) Cross section through a representative segment of the flagellum. (F) Cross section through the endpiece. (G) Representation of a 9+9+2 axoneme typically found in insect sperm. (H) Drawing of a cross section view of the axonemal doublet showing the A and B subtubules. Key: inner acrosomal rod (ar), acrosomal vesicle (av), outer extra acrosomal layer (el), centriole adjunct material (ca), axoneme (ax), mitochondrial derivatives (md), accessory bodies (ab), paracrytalline inclusions (pc), doublets (d), dynein arms (da), radial spokes (rs), microtubules (ct), central sheath (cs), accessory tubules (at), intertubular material (itm), inner dynein arm (ia), outer dynein arm (oa), mitochondrial derivative 1 (md1), and mitochondrial derivative 2 (md2). For more detailed description see reference.

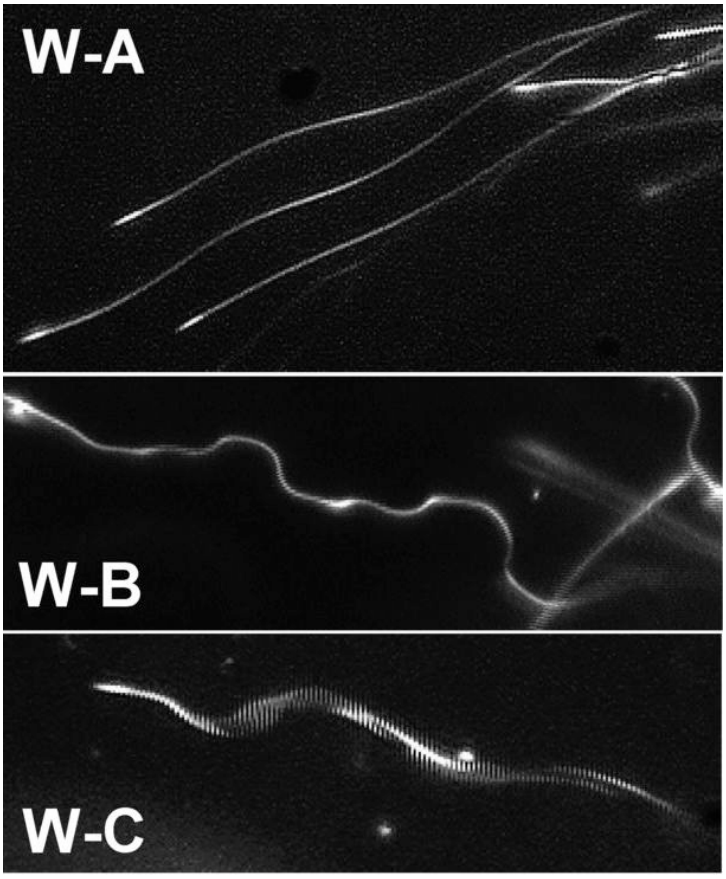

Figure 5 Sperm waveforms from *C. quinquefasciatus* (Thaler et. al., 2013). Top: waveform A, Middle: waveform B, Bottom: waveform C. Taken at 20x magnification using dark field microscopy.

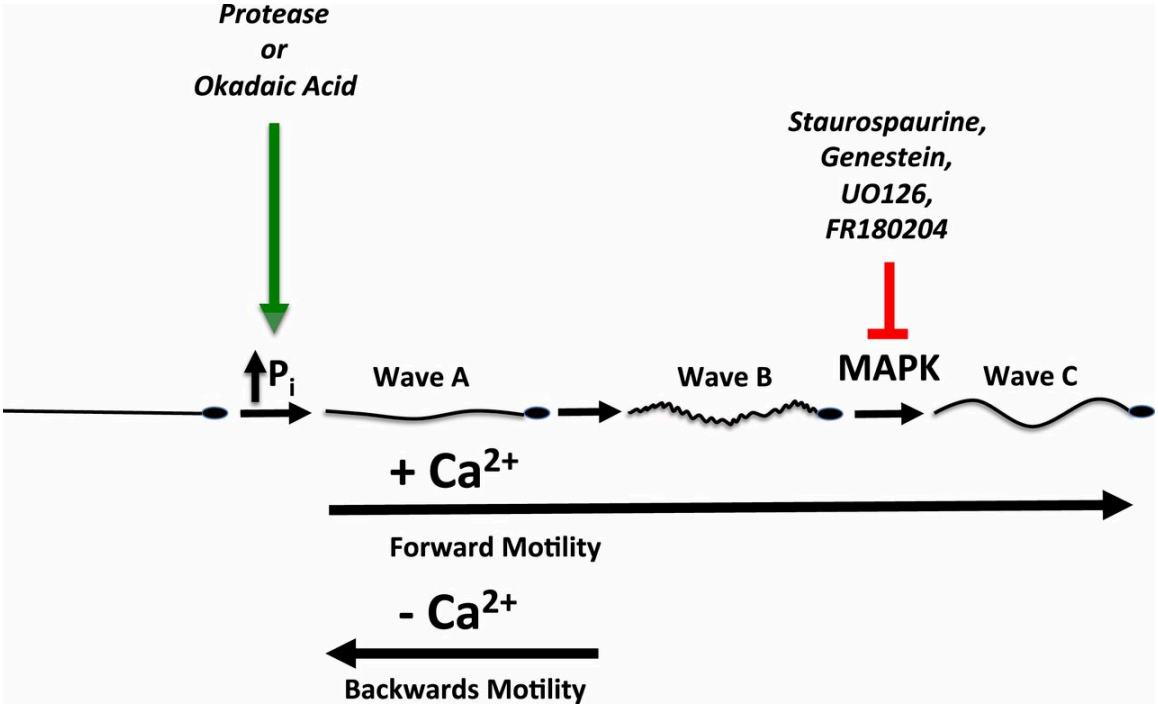

Figure 6 Activation and Regulation of Motility of *C. quinquefasciatus* (Thaler et. al., 2013). Pathway indicating forward motility regulation under conditions with increased concentration of calcium is shown by arrow pointing forward. The pathway also shows a backwards motility with removal of calcium, indicated by the backwards pointed arrow. In addition steps to the pathway showing key molecular events are pictured.

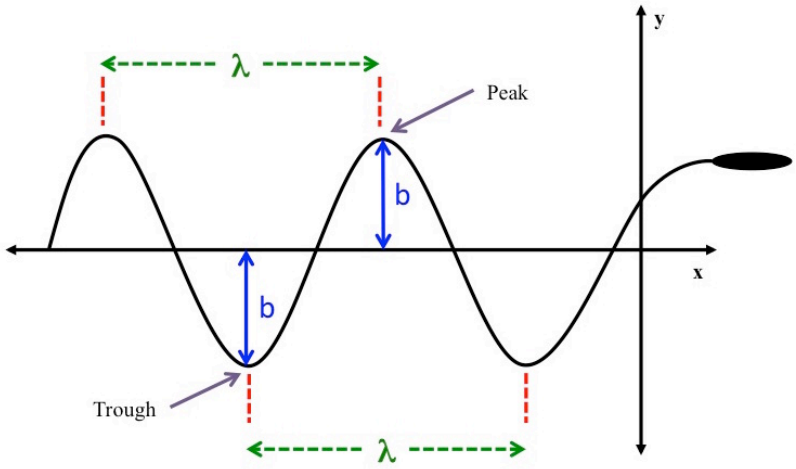

Figure 7 Sperm Key Parameter Measurements. The amplitude measured as an absolute value from the axis to the peak or the axis to the trough is shown as b. The wavelength can be measured from peak-to-peak or trough-to-trough as indicated by the red dashed lines and shown as λ green dashed lines.

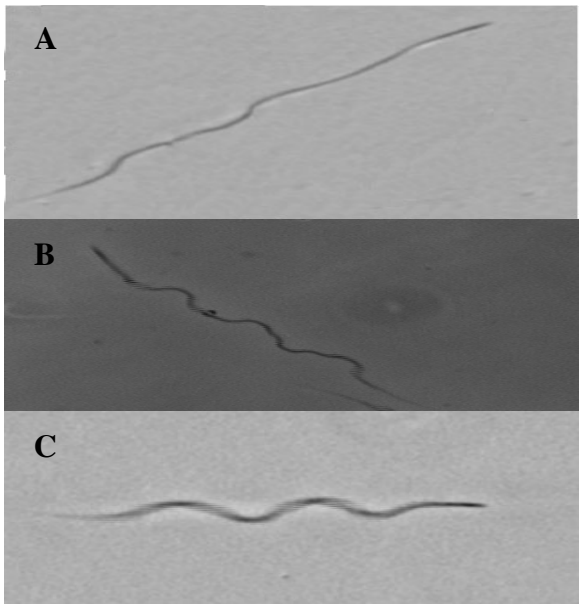

Figure 8 Waveforms in *C. pipiens* Sperm. Waveforms recorded using phase contrast microscopy at 10x magnification after dissecting *C. pipiens* male mosquitos and removing their seminal vesicles and accessory glands. The images are of sperm placed and activated on a glass slide consisting of accessory gland secretions, sperm, and insect ringer covered with a coverslip. A. Waveform A. B. Waveform B. C. Waveform C. Each sperm is taken from a different sample.

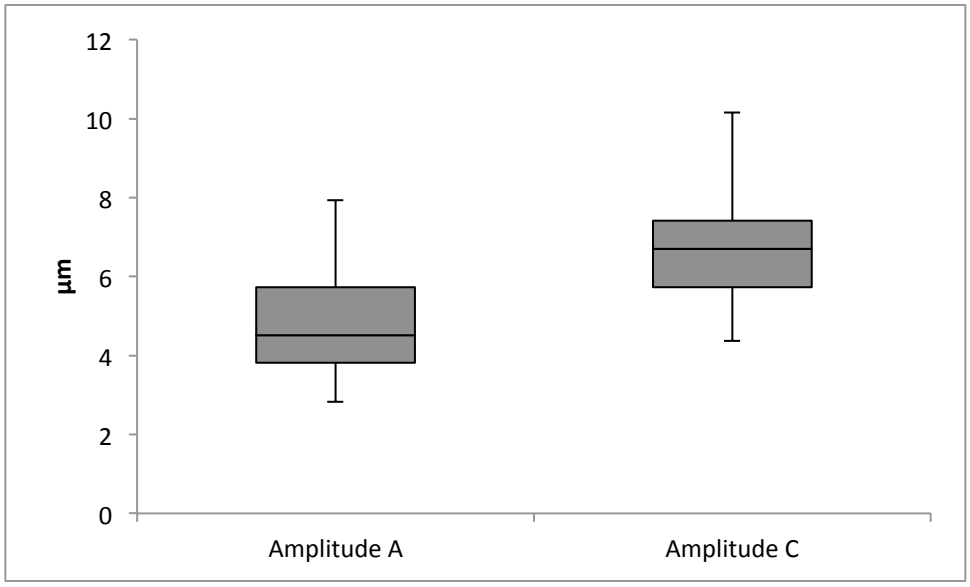

Figure 9 Amplitude of Waveform A vs. C. Amplitudes of both wave A and C were recorded at 10x magnitude using phase contrast microscopy. Analysis was performed using ImageJ.

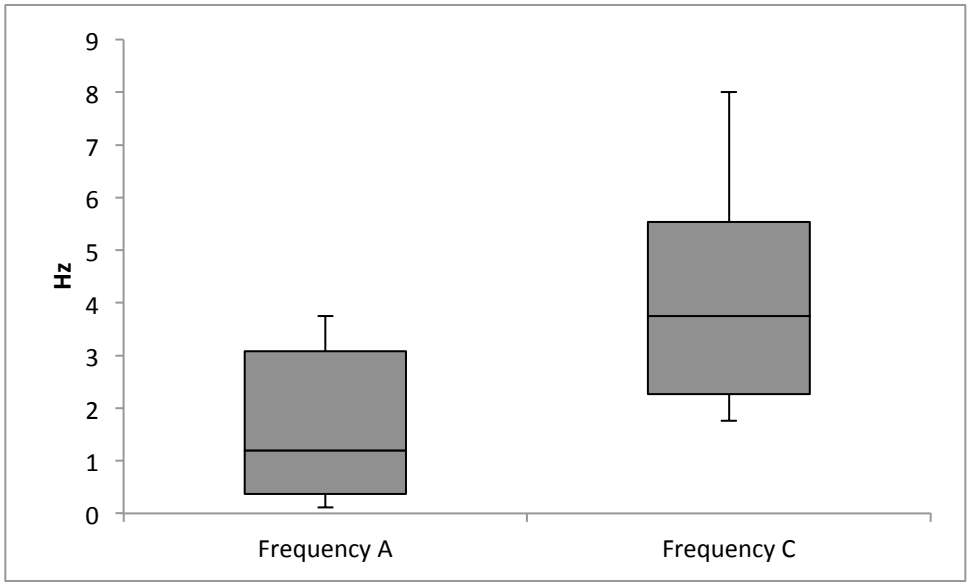

Figure 10 Frequency of Waveform A vs. C. 16 different samples showing properties that fit each waveform range were measured using ImageJ.

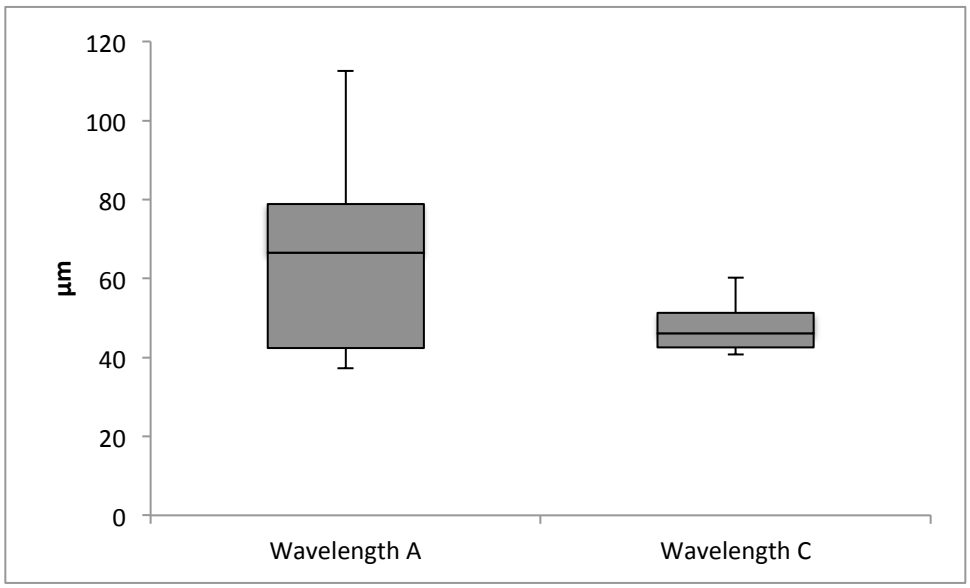

Figure 11 Wavelength of Wave A vs. Wave C. Sperm undergoing wave A and C were recorded at 10x magnitude using phase contrast microscopy. Analysis for wavelength was performed using ImageJ.

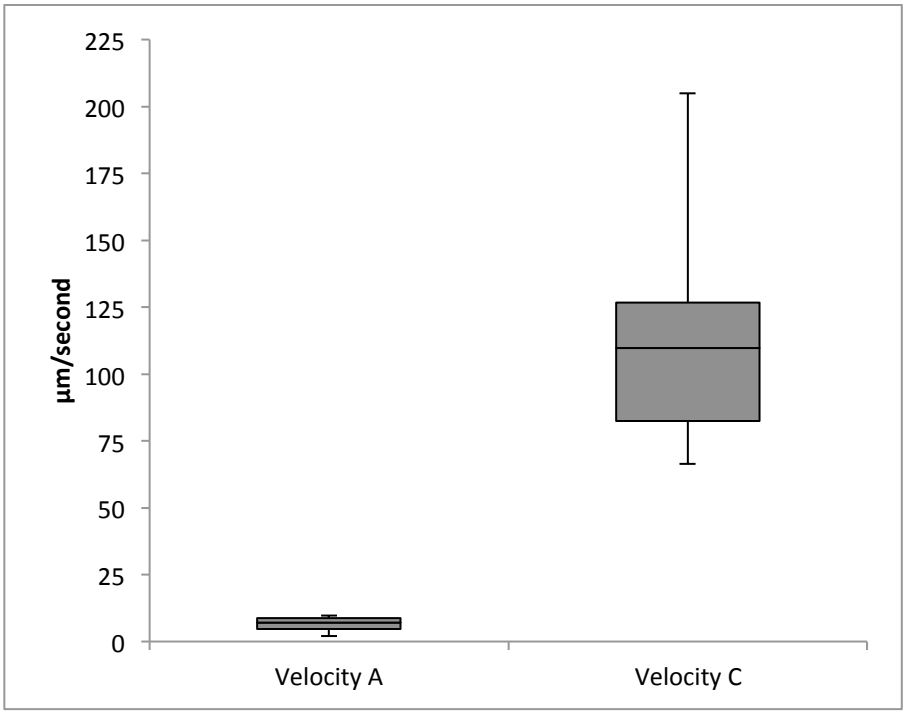

Figure 12 Velocity of Waveform A vs. C. Velocity of sperm undergoing wave A or wave C were measured and a box and whisker plot was used to display the wide range of data within each sample group and between the two sample groups. 10x magnification, phase contrast microscopy, and Image J were used to analyze sperm data from video recordings.

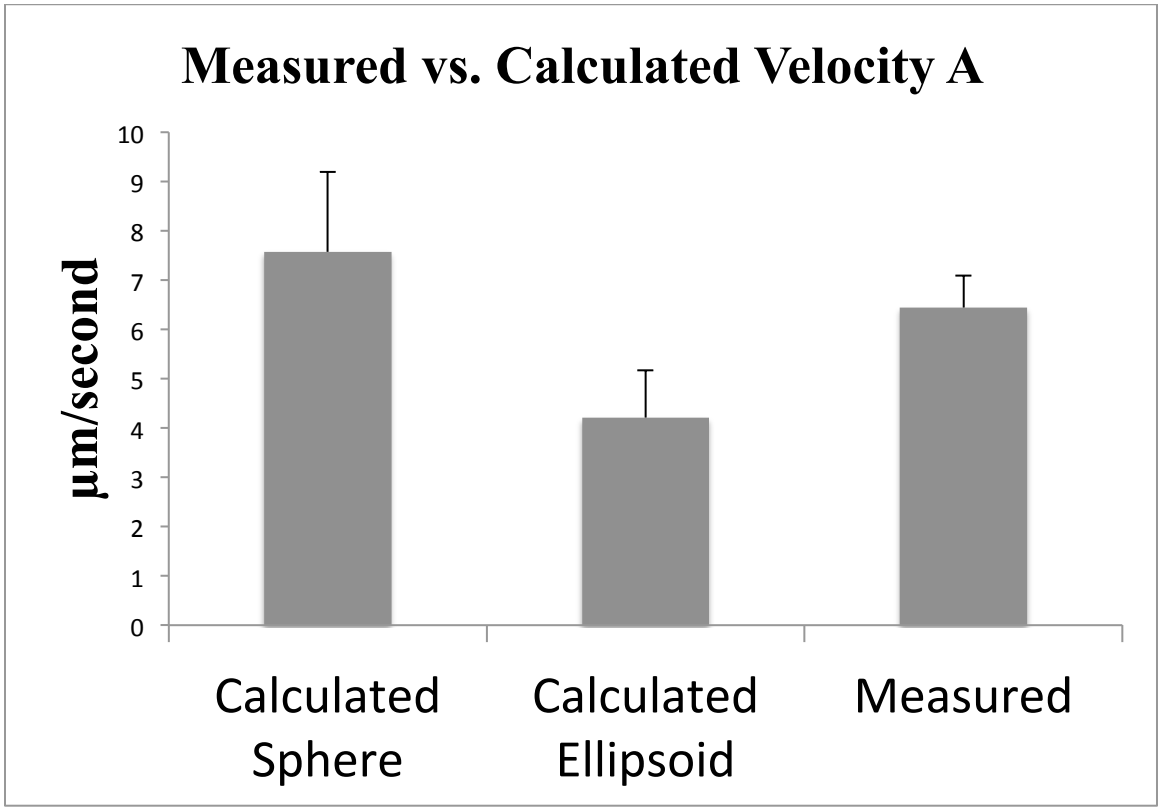

Figure 13 Comparisons of Sperm Velocity between Measured and Calculated Waveform A. calculated sphere bar corresponds to the original RFT equation proposed by Gray and Hancock (1955). Calculated ellipsoid bar corresponds to the modified equation that adjusted for an ellipsoid head of the sperm as observed using phase contrast microscopy. The measured bar represents the measured average using ImageJ to track the distance covered by the head of the sperm after at least 3 seconds worth of frames.

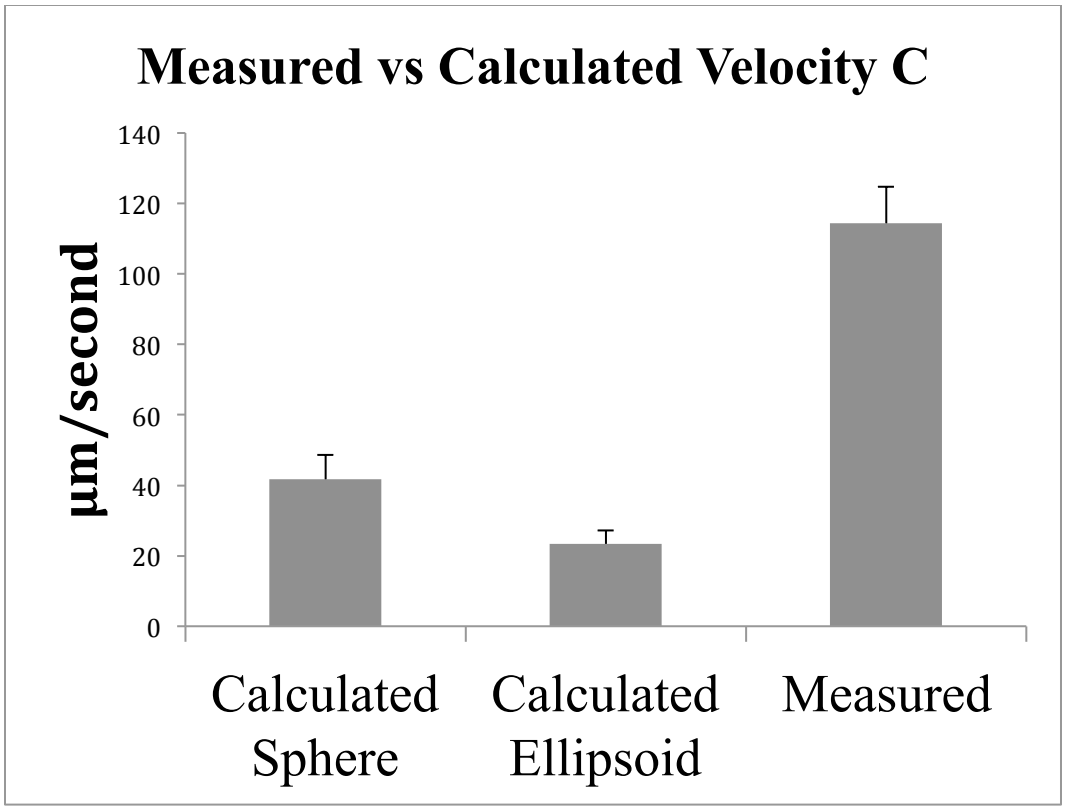

Figure 14 Comparisons of Sperm Velocity between Measured and Calculated Waveform C. Calculated sphere bar corresponds to the original RFT equation proposed by Gray and Hancock (1955). Calculated ellipsoid bar corresponds to the modified equation that adjusted for an ellipsoid head of the sperm as observed using phase contrast microscopy. The measured bar represents the measured average using ImageJ to track the distance covered by the head of the sperm after at least 3 seconds worth of frames.

7. Tables

Variable	Definition
b	Amplitude
a	Radius equivalent of an Oblate ellipsoid
d	Radius of filament
n	Number of waves exhibited by the tail
λ	Wavelength
f	Beat frequency

Table 1 Key Sperm Parameters. Variables assigned to key sperm parameters as identified by Gray and Hancock (1955) for calculating velocity of a sperm using resistive force theory.

Variable	Wave A	Wave C
b	4.84 μm ± 0.35	6.67 μm ± 0.38
a	18.5 μm	18.5 μm
d	0.95 μm ± 0.57	0.95 μm ± 0.57
n	1.09 ± 0.05	1.91 ± 0.05
λ	64.74 μm ± 5.56	47.82 μm ± 1.62
f	1.59 Hz ± 0.34	4.16 Hz ± 0.52
Observed velocity	6.44 μm/sec ± 0.65	114.31 μm/sec ± 10.41

Table 2 Measured Parameters for *C. pipiens* Sperm. Measured values of 16 different sperm for the key parameters of *C. pipiens* sperm. Measurements were done using ImageJ.

	Major (μm)	Minor (μm)
Ellipsoid Head	14.10 ± 0.55	2.09 ± 0.54

Table 3 Measures Head Morphology Parameters for *C. pipiens* Sperm. Head dimension measurements of *C. pipiens* sperm heads of 30 different samples under 20x magnification. Measurements were done using ImageJ ellipse tool. These consisted of inactive sperm.

Velocity A (μm/s)	Amplitude A (μm)	Wavelength A (μm)	Frequency A (Hz)	n_A
2.2	3.44	37.26	0.38	1.5
4.54	6.38	37.82	0.25	1
4.93	3.95	43.22	0.35	1
4.86	3.66	37.7	3	1
8.75	3.95	39.82	3.33	1.5
3.73	5.97	52.38	0.11	1
8.61	5.24	112.5	3.75	1
9.45	3.85	58.34	0.85	1.5
9.2	2.82	83.47	1.15	1
7.74	4.64	62.1	1.36	1
9.69	5.06	78.18	1.25	1
6.33	7.93	78.49	0.31	1
4.65	4.37	76.07	2.14	1
2.03	3.71	70.84	3.33	1
8.67	6.77	80.12	0.41	1
7.73	5.65	87.5	3.53	1

Table 4 Key Parameter Values for Waveform A. The values measured for all 16 samples of sperm categorized as waveform A sperm. Measurements were performed using ImageJ and phase contrast microscopy.

Velocity C (μm/s)	Amplitude C (μm)	Wavelength C (μm)	Frequency C (Hz)	n_C
86.36	6.45	42.34	2	2
102.79	5.89	41.73	2.14	2
110.84	4.75	40.72	1.76	2
66.31	7.26	42.78	3.33	2
198.04	7.89	42.54	2.31	2
205.04	6.95	43.95	2.31	2
118.12	7.37	53.5	2.14	2
69.8	5.02	50.54	3.75	1.5
70.84	4.37	60.08	4.28	2
124.31	6.1	60.22	7.5	1.5
125.61	10.15	54.19	6.67	1.5
144.07	5.25	46.65	5.29	2
97.92	6.005	45.48	6	2
70	7.1	40.86	3.75	2
108.46	7.52	50.1	5.38	2
130.42	8.71	49.48	8	2

Table 5 Key Parameter Values for Waveform C. The values measured for all 16 samples of sperm categorized as waveform A sperm. Measurements were performed using ImageJ and phase contrast microscopy.